SUPPLEMENTARY INFORMATION

doi:10.1038/nature12307

CONTENTS

I. THEORY

Optomechanical systems can be described theoretically with the Hamiltonian (see main text)

$$H = \hbar\omega_{\rm o}\hat{a}^\dagger\hat{a} + \hbar\omega_{\rm m0}\hat{b}^\dagger\hat{b} + \hbar g_0\hat{a}^\dagger\hat{a}(\hat{b}^\dagger + \hat{b}), \quad \text{(S1)}$$

where $\hat{a}$ and $\hat{b}$ are the annihilation operators for photons and phonons in the system, respectively. Generally, the system is driven by intense laser radiation at a frequency $\omega_{\rm L}$, making it convenient to work in an interaction frame where $\omega_{\rm o}$ is replaced by Δ in the above Hamiltonian with $\Delta = \omega_{\rm o} - \omega_{\rm L}$. To quantum mechanically describe the dissipation and noise from the environment, we use the quantum-optical Langevin differential equations (QLEs) [1–3],

$$\begin{aligned}\dot{\hat{a}}(t) &= -\left(i\Delta + \frac{\kappa}{2}\right)\hat{a} - ig_0\hat{a}(\hat{b}^\dagger + \hat{b}) \\ &\quad -\sqrt{\kappa_{\rm e}}\hat{a}_{\rm in}(t) - \sqrt{\kappa_{\rm i}}\hat{a}_{\rm in,i}(t), \\ \dot{\hat{b}}(t) &= -\left(i\omega_{\rm m0} + \frac{\gamma_{\rm i}}{2}\right)\hat{b} - ig_0\hat{a}^\dagger\hat{a} - \sqrt{\gamma_{\rm i}}\hat{b}_{\rm in}(t),\end{aligned}$$

which account for coupling to the bath with dissipation rates $\kappa_{\rm i}$, $\kappa_{\rm e}$, and $\gamma_{\rm i}$ for the intrinsic cavity energy decay rate, optical losses to the waveguide coupler, and total mechanical losses, respectively. The total optical losses are $\kappa = \kappa_{\rm e} + \kappa_{\rm i}$. These loss rates are necessarily accompanied by random fluctuating inputs $\hat{a}_{\rm in}(t)$, $\hat{a}_{\rm in,i}(t)$, and $\hat{b}_{\rm in}(t)$, for optical vacuum noise coming from the coupler, optical vacuum noise coming from other optical loss channels, and mechanical noise (including thermal).

The study of squeezing is a study of noise propagation in the system of interest and as such, a detailed understanding of the noise properties is required. The equations above are derived by making certain assumptions about the noise, and are generally true for the case of an optical cavity, where thermal noise is not present, and where we are interested only in a bandwidth of roughly 10^8 smaller than the optical frequency (0 – 40 MHz bandwidth of a 200 THz resonator). For the mechanical system, where we operate at very large thermal bath occupancies ($\gg 10^3$) and are interested in the broadband

* These authors contributed equally to this work.
† opainter@caltech.edu; http://copilot.caltech.edu

properties of noise sources (0 – 40 MHz for a 30 MHz resonator), a more detailed understanding of the bath is required, and will be presented in the section on thermal noise.

At this point, we linearize the equations assuming a strong coherent drive field α_0, and displace the annihilation operator for the photons by making the transformation $\hat{a} \to \alpha_0 + \hat{a}$. This approximation, which neglects terms of order $\hat{a}^2$ is valid for systems such as ours where $g_0 \ll \kappa$, i.e. the *vacuum weak coupling* regime. We are then left with a parametrically enhanced coupling rate $G = g_0|\alpha_0|$. Using the relations given in the mathematical definitions section (VI) of this document, we write the solution to the QLEs in the Fourier domain as

$$\hat{a}(\omega) = \frac{-\sqrt{\kappa_\mathrm{e}}\hat{a}_\mathrm{in}(\omega) - \sqrt{\kappa_\mathrm{i}}\hat{a}_\mathrm{in,i}(\omega) - iG(\hat{b}(\omega) + \hat{b}^\dagger(\omega))}{i(\Delta - \omega) + \kappa/2},$$

$$\hat{b}(\omega) = \frac{-\sqrt{\gamma_\mathrm{i}}\hat{b}_\mathrm{in}(\omega)}{i(\omega_\mathrm{m0} - \omega) + \gamma_\mathrm{i}/2} - \frac{iG(\hat{a}(\omega) + \hat{a}^\dagger(\omega))}{i(\omega_\mathrm{m0} - \omega) + \gamma_\mathrm{i}/2}. \quad \text{(S2)}$$

(We use the notation described in section VI where $\left(\hat{A}(\omega)\right)^\dagger = \hat{A}^\dagger(-\omega)$.)

Finally we note that by manipulation of these equations, the mechanical motion can be expressed as a (renormalized) response to the environmental noise and the optical vacuum fluctuations incident on the optical cavity through the optomechanical coupling

$$\begin{aligned}\hat{b}(\omega) = &\frac{-\sqrt{\gamma_\mathrm{i}}\hat{b}_\mathrm{in}(\omega)}{i(\omega_\mathrm{m} - \omega) + \gamma/2} \\ &+ \frac{iG}{i(\Delta - \omega) + \kappa/2}\frac{\sqrt{\kappa_\mathrm{e}}\hat{a}_\mathrm{in}(\omega) + \sqrt{\kappa_\mathrm{i}}\hat{a}_\mathrm{in,i}(\omega)}{i(\omega_\mathrm{m} - \omega) + \gamma/2} \\ &+ \frac{iG}{-i(\Delta + \omega) + \kappa/2}\frac{\sqrt{\kappa_\mathrm{e}}\hat{a}^\dagger_\mathrm{in}(\omega) + \sqrt{\kappa_\mathrm{i}}\hat{a}^\dagger_\mathrm{in,i}(\omega)}{i(\omega_\mathrm{m} - \omega) + \gamma/2}.\end{aligned} \quad \text{(S3)}$$

The renormalized mechanical frequency and loss rate are $\omega_\mathrm{m} = \omega_\mathrm{m0} + \delta\omega_\mathrm{m}$, and $\gamma = \gamma_\mathrm{i} + \gamma_\mathrm{OM}$, respectively, with

$$\delta\omega_\mathrm{m} = |G|^2 \mathrm{Im}\left[\frac{1}{i(\Delta - \omega_\mathrm{m}) + \kappa/2} - \frac{1}{-i(\Delta + \omega_\mathrm{m}) + \kappa/2}\right], \quad \text{(S4)}$$

$$\gamma_\mathrm{OM} = 2|G|^2 \mathrm{Re}\left[\frac{1}{i(\Delta - \omega_\mathrm{m}) + \kappa/2} - \frac{1}{-i(\Delta + \omega_\mathrm{m}) + \kappa/2}\right]. \quad \text{(S5)}$$

It is convenient to define here what we mean by a quadrature, as it is the observable of the light field that our measurement device (the balanced homodyne detector (BHD) setup) is sensitive to:

$$\hat{X}^{(j)}_\theta(t) = \hat{a}_j(t)e^{-i\theta} + \hat{a}^\dagger_j(t)e^{i\theta}. \quad j = \mathrm{in}, \mathrm{out}, \mathrm{vac}, .. \quad \text{(S6)}$$

We are interested in the properties of $\hat{X}^{(\mathrm{out})}_\theta$ for various quadrature angles θ, given the influence of the mechanical system.

The measurement of the field provides us with a record $\hat{I}(t) = \hat{X}^{(\mathrm{out})}_\theta(t)$ for a certain θ. We use a spectrum analyzer to perform Fourier analysis on this signal and obtain a symmetrized classical power spectral density (PSD) $\bar{S}_{II}(\omega)$, as defined in the mathematical appendix (section VI).

For a vacuum field such as the input field, the measured quadrature $\hat{X}^{(\mathrm{vac})}_\theta(t)$ will have a power spectral density

$$\bar{S}^{\mathrm{vac}}_{II}(\omega) = 1. \quad \text{(S7)}$$

This is the shot-noise level which is due to the quantum fluctuations of the electromagnetic field. Mathematically, it arises from the correlator $\langle \hat{a}_\mathrm{vac}(\omega)\hat{a}^\dagger_\mathrm{vac}(\omega')\rangle = \delta(\omega + \omega')$, with all other correlators $\langle \hat{a}^\dagger_\mathrm{vac}(\omega)\hat{a}_\mathrm{vac}(\omega')\rangle$, $\langle \hat{a}^\dagger_\mathrm{vac}(\omega)\hat{a}^\dagger_\mathrm{vac}(\omega')\rangle$, $\langle \hat{a}_\mathrm{vac}(\omega)\hat{a}_\mathrm{vac}(\omega')\rangle$, arising in the expression $\langle \hat{I}^\dagger(\omega)\hat{I}(\omega')\rangle$ equal to zero.

A. Approximate quasi-static theory

In this section we present a simplified derivation of how squeezing is obtained in the studied optomechanical system to elucidate the important system parameters and their role in squeezing. We make a few approximations to simplify the derivation:

1. $\Delta = 0$: The laser is tuned exactly to the optical cavity frequency.
2. $\kappa_\mathrm{e} = \kappa$: Perfect coupling.
3. $\kappa \gg \omega_\mathrm{m}$: Bad cavity limit.
4. $\omega \ll \omega_\mathrm{m}$: We are only interested in the quasi-static response, so the resonant response of the mechanical resonator does not play a role.

Under these assumptions, equations (S2) and (S3) can be written as (using the relation for the optical output field $\hat{a}_\mathrm{out}(\omega) = \hat{a}_\mathrm{in}(\omega) + \sqrt{\kappa}\hat{a}(\omega)$):

$$\begin{aligned} i\omega_\mathrm{m}\hat{b}(\omega) &= -\sqrt{\gamma_\mathrm{i}}\hat{b}_\mathrm{in}(\omega) + \frac{2iG}{\sqrt{\kappa}}(\hat{a}_\mathrm{in}(\omega) + \hat{a}^\dagger_\mathrm{in}(\omega)), \\ \hat{a}_\mathrm{out}(\omega) &= -\hat{a}_\mathrm{in}(\omega) - \frac{2iG}{\sqrt{\kappa}}(\hat{b}(\omega) + \hat{b}^\dagger(\omega)). \end{aligned} \quad \text{(S8)}$$

The first equation shows the response of the mechanical resonator subsystem to the thermal bath fluctuations ($\hat{b}_\mathrm{in}(\omega)$) and the optical vacuum noise from the measurement back-action. We define $\Gamma_\mathrm{meas} \equiv 4|G|^2/\kappa$, and interpret it as the measurement rate [4], such that the factor appearing in front of the optical vacuum noise operators is $\sqrt{\Gamma_\mathrm{meas}}$. This rate also appears in the second equation for the output field, in front of the normalized position operator $\hat{x}/x_\mathrm{zpf} = \hat{b}(\omega) + \hat{b}^\dagger(\omega)$, which is the observable that is being measured.

Note, from the expression for $\hat{a}_\mathrm{out}(\omega)$ it follows, that since the position is a real observable with an imaginary prefactor, the effects we consider depend strongly on the

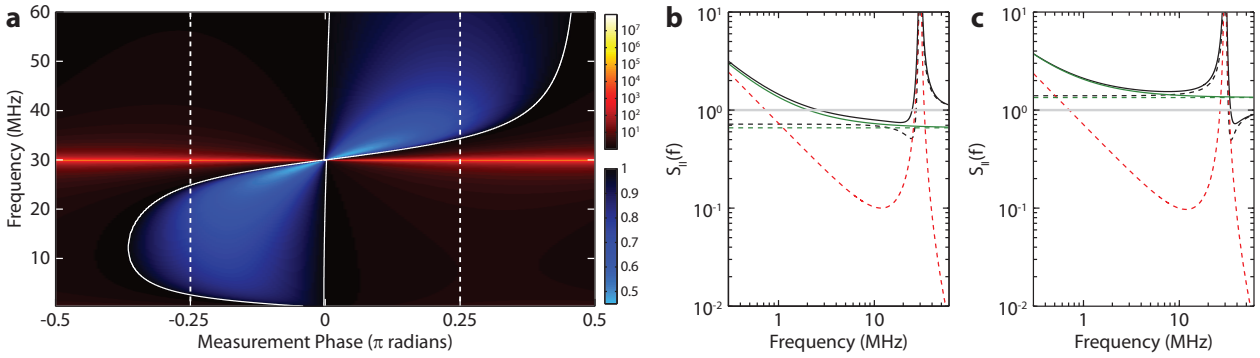

FIG. S1. **Squeezing theory.** **a**, Density plot of the predicted squeezing $\bar{S}^{\rm out}_{II}(\omega)$ vs. phase angle and frequency, normalized to the shot-noise. The mechanical mode can clearly be seen at $\omega_{\rm m}/2\pi = 30$ MHz. The solid white lines outline the region where the power spectral density falls below 1 (the shot-noise level) indicating the presence of squeezing for that phase and frequency. The dashed white lines at $\theta = -\pi/4$ and $\theta = +\pi/4$ correspond to regions where squeezing can be obtained below and above the mechanical frequency, respectively, and the components of the noise model for these phases is shown in detail in figures **b** and **c**. In these figures the spectra are again normalized to the shot-noise level plotted as a grey line. The simple squeezing model without thermal noise (Eq. (S10)) is represented by the dashed green line and the simple model with thermal noise (Eq. (S18)) is the solid green line. The solid black line is the full squeezing model $\bar{S}^{\rm out}_{II}(\omega)$ corresponding to **a** with the constituent components: the contribution from the optical vacuum fluctuations ($\bar{S}^{\rm out}_{II,a}(\omega)$; Eq. (S25)) represented by the dashed black line and the thermal noise ($\bar{S}^{\rm out}_{II,b}(\omega)$; Eq. (S26)) represented by the dashed red line.

quadrature being probed, i.e. the real part of the expression, $\hat{X}^{(\rm out)}_{\theta=0}$, will not be affected by the optomechanical coupling.

At this point we can easily calculate the properties of the detected spectrum $\bar{S}^{\rm out}_{II}(\omega)$, by writing $\hat{a}_{\rm out}$ in terms of $\hat{a}_{\rm in}$ and $\hat{b}_{\rm in}$ for which the correlators are known:

$$\hat{a}_{\rm out}(\omega) = -\hat{a}_{\rm in}(\omega) - 2i\frac{\Gamma_{\rm meas}}{\omega_{\rm m}}(\hat{a}_{\rm in}(\omega) + \hat{a}^{\dagger}_{\rm in}(\omega)) + \frac{\sqrt{\gamma_{\rm i}\Gamma_{\rm meas}}}{\omega_{\rm m}}(\hat{b}_{\rm in}(\omega) - \hat{b}^{\dagger}_{\rm in}(\omega)). \quad \text{(S9)}$$

Ignoring thermal noise for the moment ($\gamma_{\rm i} = 0$), and dropping terms of order $(\Gamma_{\rm meas}/\omega_{\rm m})^2$ (assuming $\Gamma_{\rm meas} \ll \omega_{\rm m}$) we arrive at:

$$\bar{S}^{\rm out}_{II}(\omega) = \int_{-\infty}^{\infty} d\omega' \ \langle \hat{X}^{(\rm out)}_{\theta}(\omega)\hat{X}^{(\rm out)}_{\theta}(\omega')\rangle = 1 + 4(\Gamma_{\rm meas}/\omega_{\rm m})\sin(2\theta). \quad \text{(S10)}$$

Note that for certain values of θ, the detected spectral density can be smaller than what one would expect for a vacuum field. For $\theta = -\pi/4$, we achieve the maximum squeezing with a noise floor of $1 - 4(\Gamma_{\rm meas}/\omega_{\rm m})$ which strongly dependends on the ratio $\Gamma_{\rm meas}/\omega_{\rm m}$.

To understand the effect of thermal noise, we assume the form of the correlator to be $\langle \hat{b}_{\rm in}(\omega)\hat{b}^{\dagger}_{\rm in}(\omega')\rangle = (\bar{n}(\omega)+1)\delta(\omega+\omega')$, $\langle \hat{b}^{\dagger}_{\rm in}(\omega)\hat{b}_{\rm in}(\omega')\rangle = \bar{n}(\omega)\delta(\omega+\omega')$, $\langle \hat{b}^{\dagger}_{\rm in}(\omega)\hat{b}^{\dagger}_{\rm in}(\omega')\rangle = 0$, and $\langle \hat{b}_{\rm in}(\omega)\hat{b}_{\rm in}(\omega')\rangle = 0$ (these expressions are discussed in section IV H). Then a calculation similar to the one leading to equation (S10) gives

$$\bar{S}^{\rm out}_{II}(\omega) = 1 + 4(\Gamma_{\rm meas}/\omega_{\rm m})\sin(2\theta) + 4\frac{\Gamma_{\rm meas}}{\omega_{\rm m}}\frac{\bar{n}(\omega)}{Q_m}(1-\cos(2\theta)), \quad \text{(S11)}$$

where we have assumed $\bar{n}(\omega)$, the bath occupation at frequency ω, to be much larger than unity. At $\theta = -\pi/4$, we have

$$\bar{S}^{\rm out}_{II}(\omega) = 1 - 4(\Gamma_{\rm meas}/\omega_{\rm m})(1 - \bar{n}(\omega)/Q_m). \quad \text{(S12)}$$

In this model, there is no squeezing at $\theta = -\pi/4$ and frequency ω if $\bar{n}(\omega) > Q_m$. Some squeezing is always present, but is shifted to other quadratures and the amount of detectable squeezing is reduced at higher temperatures. Most of the squeezing (59%) is washed out by the thermal noise at $\bar{n}(\omega) = Q_m$. The squeezing arises from the time evolution of the mechanical resonator maintaining coherence over the time scale of the fluctuations. Requiring coherent evolution over the mechanical cycle is equivalent to demanding that the rate at which phonons enter the mechanical system from the bath ($\gamma_{\rm i}\bar{n}$) to be smaller than the mechanical frequency $\omega_{\rm m}$. In conclusion, the important requirements to achieve squeezing are to make $\Gamma_{\rm meas}$ comparable to $\omega_{\rm m}$ and to reduce the thermal occupancy or increase the mechanical quality factor to achieve $\bar{n}(\omega) \lesssim Q_m$.

B. The effect of dynamics and correlation between RPSN and position

As a next step, we take into account the dynamics of the mechanical resonator while keeping the approximations of the bad-cavity limit ($\kappa \gg \omega_{\rm m}$) and on-resonant probing ($\Delta = 0$). In addition to further clarifying some of the observed features, this treatement, as presented in the main text, elucidates the role of correlations be-

tween the mechanical system's position and the back-action force.

The response of the mechanical system to a force is captured by its susceptibility:

$$\chi_{\rm m}(\omega) = \frac{1}{m(\omega_{\rm m}^2 - \omega^2 - i\gamma_{\rm i}\omega_{\rm m})}. \quad \text{(S13)}$$

The form of the damping considered here is the strongly sub-ohmic structural damping which is observed in our measurements [5, 6] (cf. Section IV H). The mechanical system responds to random noise forces $F_{\rm T}(t)$ from the thermal bath (which we treated in the last section and neglect here), and to the quantum back-action from the cavity $F_{\rm BA}(t)$.

The back-action force for the resonant case can simply be found by linearizing the expression for the radiation pressure force $\hat{F}_{\rm RP}(t) = -\hbar g_0 \hat{a}^\dagger \hat{a}/x_{\rm zpf}$. We find the force imparted on the mechanics due to the shot-noise of the cavity field to be

$$\hat{F}_{\rm BA}(t) = \frac{\hbar \cdot \sqrt{\Gamma_{\rm meas}}}{x_{\rm zpf}} \hat{X}^{\rm (in)}_{\theta=0}(t) \quad \text{(S14)}$$

for the case of resonant driving. The fluctuations imparted on the mechanics are from the intensity quadrature of the light ($\theta = 0$). Using equation (S8), we can write the output field quadrature as:

$$\hat{X}^{\rm (out)}_{\theta}(t) = -\hat{X}^{\rm (in)}_{\theta}(t) - 2\frac{\sqrt{\Gamma_{\rm meas}}}{x_{\rm zpf}} \hat{x}(t) \cdot \sin(\theta). \quad \text{(S15)}$$

We note here that the mechanical position fluctuations are primarily imprinted on the phase quadrature of the output light, with $\theta = \pm\pi/2$. The intensity quadrature is unmodified ($\hat{X}^{\rm (out)}_{\theta=0}(t) = -\hat{X}^{\rm (in)}_{\theta=0}(t)$) since changes in the cavity frequency are not transduced as changes in intensity when the laser is resonant with the cavity.

The output of the homodyne detector normalized to the shot-noise level is found by taking the autocorrelation of eqn. (S15). The correlations between radiation pressure shot-noise and the mechanical motion are important in this calculation [7–13] and must be taken into account. In the time-domain we find the autocorrelation to be:

$$\langle \hat{X}^{\rm (out)}_{\theta}(t)\hat{X}^{\rm (out)}_{\theta}(t')\rangle = \delta(t-t') + 4\Gamma_{\rm meas}\sin^2(\theta)\frac{\langle \hat{x}(t)\hat{x}(t')\rangle}{x_{\rm zpf}^2} + 2\hbar^{-1}\sin(\theta)\cos(\theta)\langle \hat{F}_{\rm BA}(t)\hat{x}(t') + \hat{x}(t)\hat{F}_{\rm BA}(t')\rangle. \quad \text{(S16)}$$

The $\cos(\theta)$ in the last term comes from the general expression for a quadrature $\hat{X}^{\rm (in)}_{\theta}(t) = \hat{X}^{\rm (in)}_{\theta=0}(t)\cos(\theta) + \hat{X}^{\rm (in)}_{\theta=\pi/2}(t)\sin(\theta)$, and equation (S14). The key components of equation (S16) are the shot-noise level, the thermal noise, and the cross-correlation between the back-action noise force and mechanical position fluctuations. It is only the latter which can give rise to squeezing, by reducing the fluctuation level below shot-noise. This squeezing can be calculated spectrally:

$$\begin{aligned} S_{\rm sq}(\omega) &= \hbar^{-1}\sin(2\theta) \times \int_{-\infty}^{\infty} {\rm d}\tau [\langle \hat{F}_{\rm BA}(t)\hat{x}(t-\tau)\rangle \\ &\quad + \langle \hat{x}(t)\hat{F}_{\rm BA}(t-\tau)\rangle] e^{i\omega\tau} \\ &= 2\hbar {\rm Re}\left\{\chi_{\rm m}(\omega)\right\}\Gamma_{\rm meas}/x_{\rm zpf}^2 \sin(2\theta). \end{aligned} \quad \text{(S17)}$$

The full detected spectral density is then

$$\bar{S}^{\rm out}_{II}(\omega) = 1 + \frac{4\Gamma_{\rm meas}}{x_{\rm zpf}^2}\left[\bar{S}_{xx}\sin^2(\theta) + \frac{\hbar}{2}{\rm Re}\{\chi_{\rm m}\}\sin(2\theta)\right]. \quad \text{(S18)}$$

At the DC or quasi-static limit ($\omega \to 0$) the susceptibility $\chi_{\rm m} \to 1/m\omega_{\rm m}^2$ can be used and we reobtain the results from section I A (cf. equation (S10)). We see that for $\theta < 0$, squeezing is obtained in this limit. At frequencies larger than $\omega_{\rm m}$, $\chi_{\rm m}(\omega)$ changes sign, and we expect to see squeezing at quadrature angles $\theta > 0$. Additionally, since $\chi_{\rm m}(\omega)$ becomes larger around the mechanical frequency, we expect the maximum squeezing to be enhanced. More specifically, at a detuning $\delta = \omega_m - \omega$ ($|\delta| \gg \gamma_{\rm i}$) from the mechanical resonance, we expect the parameter characterizing the squeezing to be proportional to $\Gamma_{\rm meas}/\delta$, and the detected spectrum shown in equation (S18) becomes $\bar{S}^{\rm out}_{II}(\omega > 0) \approx 1 + (2\Gamma_{\rm meas}/\delta)[(\omega_{\rm m}/\delta)(\bar{n}(\omega)/Q_{\rm m})(1-\cos(2\theta)) + \sin(2\theta)]$. These features are evident in the spectra presented in Fig. S1.

It is important to note here that in the absence of other nonlinearities in the system, any reduction of the noise below the vacuum fluctuations can only be caused by the correlations between the RPSN and the position fluctuations of the system. This makes the problem of proving the correlations between RPSN and mechanical motion equivalent to the problem of proving that the reflected light from the optomechanical cavity is squeezed.

Conceptually this form of probing the RPSN is similar to that carried out by Safavi-Naeini et al. [10, 13] and analyzed by Khalili et al. [11]. It also shares features with the cross-correlation measurements proposed by Heidmann et al. [7], and Børkje et al. [9], and recent experiments by Purdy et al. [14]. The distinguishing feature of this type of measurement is that the quantum correlations between the fluctuations of the position and the electromagnetic vacuum manifest themselves as squeezed

light.

The effects of RPSN also play a role in the second term of equation (S18). Part of the position fluctuation power spectral density $\bar{S}_{xx}(\omega)$ can be attributed to the motional heating due to RPSN, an effect first measured in a solid state system by Purdy et al. [14]. In our measurements, at the largest powers (∼3,100 intracavity photons), roughly 65% of the displacement fluctuations are thermal, while 32% are due to RPSN heating. An additional 2% heating arises from the phase noise of the laser.

C. General derivation of squeezing

Among the approximations made in section I A, the quasi-static approximation is the least correct. In fact, in our experiments, the most observable squeezing occurs with ω close to $\omega_{\rm m}$ and even slightly larger than $\omega_{\rm m}$, so $\omega \ll \omega_{\rm m}$ is not valid. Near the mechanical frequency, resonant enhancement of the optical vacuum fluctuations by the mechanical resonator causes squeezing greater than that predicted in the quasi-static regime to be possible.

Here we show the results of a derivation that does not rely on most of the assumptions used in the approximate model. Of the assumptions in the previous section, the only simplification we keep here is to assume perfect coupling $\kappa_{\rm e} = \kappa$. The effect of imperfect coupling can be taken into account trivially and is explained after this section (see I C 1).

By substitution of equation (S3) into the equation for $\hat{a}(\omega)$ (S2), we arrive at:

$$\sqrt{\kappa}\hat{a}(\omega) = A_1(\omega)\hat{a}_{\rm in}(\omega) + A_2(\omega)\hat{a}^\dagger_{\rm in}(\omega) + B_1(\omega)\hat{b}_{\rm in}(\omega) + B_2(\omega)\hat{b}^\dagger_{\rm in}(\omega), \quad \text{(S19)}$$

with

$$A_1(\omega) = \frac{\kappa}{i(\Delta-\omega)+\kappa/2} \times \left[\frac{|G|^2}{i(\Delta-\omega)+\kappa/2}\frac{1}{i(\omega_{\rm m}-\omega)+\gamma/2} - \frac{|G|^2}{i(\Delta-\omega)+\kappa/2}\frac{1}{-i(\omega_{\rm m}+\omega)+\gamma/2} - 1\right] \quad \text{(S20)}$$

$$A_2(\omega) = \frac{\kappa}{i(\Delta-\omega)+\kappa/2} \times \left[\frac{|G|^2}{-i(\Delta+\omega)+\kappa/2}\frac{1}{i(\omega_{\rm m}-\omega)+\gamma/2} - \frac{|G|^2}{-i(\Delta+\omega)+\kappa/2}\frac{1}{-i(\omega_{\rm m}+\omega)+\gamma/2}\right] \quad \text{(S21)}$$

$$B_1(\omega) = \frac{\sqrt{\kappa\gamma_{\rm i}}}{i(\Delta-\omega)+\kappa/2}\left[\frac{iG}{i(\omega_{\rm m}-\omega)+\gamma/2}\right] \quad \text{(S22)}$$

$$B_2(\omega) = \frac{\sqrt{\kappa\gamma_{\rm i}}}{i(\Delta-\omega)+\kappa/2}\left[\frac{iG}{-i(\omega_{\rm m}+\omega)+\gamma/2}\right] \quad \text{(S23)}$$

These expressions give us the output field in terms of the input fields, since

$$\begin{aligned}\hat{a}_{\rm out}(\omega) &= \hat{a}_{\rm in}(\omega) + \sqrt{\kappa}\hat{a}(\omega)) \\ &= (1+A_1(\omega))\hat{a}_{\rm in}(\omega) + A_2(\omega)\hat{a}^\dagger_{\rm in}(\omega) \\ &\quad + B_1(\omega)\hat{b}_{\rm in}(\omega) + B_2(\omega)\hat{b}^\dagger_{\rm in}(\omega). \end{aligned} \quad \text{(S24)}$$

We can calculate $\bar{S}^{\rm out}_{II}(\omega)$ from this expression, which we split into two parts, one only due to the optical vacuum fluctuations, and the other containing the contribution from thermal noise: $\bar{S}^{\rm out}_{II}(\omega) = \bar{S}^{\rm out}_{II,a}(\omega) + \bar{S}^{\rm out}_{II,b}(\omega)$.

$$\bar{S}^{\rm out}_{II,a}(\omega) = |A_2(-\omega)|^2 + |1+A_1(\omega)|^2 + 2{\rm Re}\{e^{-2i\theta}(1+A_1(\omega))A_2(-\omega)\} \quad \text{(S25)}$$

$$\begin{aligned}\bar{S}^{\rm out}_{II,b}(\omega) &= |B_1(\omega)|^2(\bar{n}(\omega)+1) + |B_1(-\omega)|^2\bar{n}(\omega) \\ &\quad + |B_2(-\omega)|^2(\bar{n}(\omega)+1) + |B_2(\omega)|^2\bar{n}(\omega) \\ &\quad + 2{\rm Re}\{e^{-2i\theta}B_1(\omega)B_2(-\omega)\}(\bar{n}(\omega)+1) + 2{\rm Re}\{e^{-2i\theta}B_1(-\omega)B_2(\omega)\}\bar{n}(\omega) \end{aligned} \quad \text{(S26)}$$

1. *The effect of imperfect optical coupling and inefficient detection*

At every juncture in an experiment where the optical transmission efficiency is less than unity ($\eta < 1$), an equivalent optical circuit can be defined involving an

$\eta : (1-\eta)$ beam splitter with the output being η times the input and $(1-\eta)$ times the vacuum. Therefore the effect of optical losses and coupling inefficiencies on the detected spectra can be calculated by replacing the measured field quadrature with:

$$\hat{X}_\theta^{(\mathrm{det})} = \sqrt{\eta}\hat{X}_\theta^{(\mathrm{out})} + \sqrt{1-\eta}\hat{X}_\theta^{(\mathrm{vac})} \qquad \text{(S27)}$$

This source of vacuum noise is completely unrelated to the cavity output, and there are no cross-correlation terms, so the detected current spectral density will be given by

$$\bar{S}_{II}^{\mathrm{det}}(\omega) = \eta\bar{S}_{II}^{\mathrm{out}}(\omega) + (1-\eta)\bar{S}_{II}^{\mathrm{vac}}(\omega), \qquad \text{(S28)}$$

where $\bar{S}_{II}^{\mathrm{vac}}(\omega) = 1$ is the shot-noise.

Measurement inefficiencies take two forms, one is due to ineffeciencies in the detection, while the second is because of excess electronic noise or "dark current" present due to the circuitry of the detector and amplifier. This excess noise can also be thought of as a detection inefficiency by considering the amount of optical shot-noise inserted into the signal which would produce it. Since the dark-current is measured with no optical input, and the real shot-noise level increases linearly with the local oscillator (LO) power, this inefficiency is power dependent and can be minimized for large LO powers. In our case, the dark current was found to be 10.4 dB below the detected shot-noise. The total detector efficiency was measured to be $\eta_{\mathrm{HD}} = 66\%$.

II. EXPERIMENT

A. Measurement of losses

In order to estimate the total squeezing expected in our setup we carefully characterize all losses in our system. Some of these losses are static (e.g. circulator losses) while others can vary from experiment to experiment (e.g. coupling efficiency of the fiber taper to the waveguide). In figure S2 typical losses are shown as efficiencies (η) for various parts of the experiment. The efficiency of sending light from port 1 to 2 of our optical circulator is $\eta_{12} = 85\%$, and $\eta_{23} = 88\%$ for port 2 to 3. In addition, the efficiency from port 3 of the circulator to the homodyne detector is $\eta_{3\mathrm{H}} = 92\%$. All these losses are fixed and do not change over time as the components are optically spliced together. Measuring the coupling efficiency of the fiber taper to the waveguide is done every time a new data set is taken. This is accomplished by switching the light that is reflected from the waveguide to a power meter and comparing the reflected power to a known input power with the laser tuned off-resonance from the optical mode (off-resonance the device acts as a near-perfect mirror). Typical achieved efficiencies are around $\eta_{\mathrm{CP}} = 90\%$. The efficiency of the homodyne detection strongly depends on the alignment of the polarization between the local oscillator and the signal, as well as by how much the power in the LO overcomes the electronic noise floor of the detector. To determine this efficiency we use an acousto-optic modulator (AOM) inserted in our setup before the circulator in the signal path. The AOM shifts the frequency of the light creating a tone 88 MHz away from the signal with a fixed, known amplitude, and identical polarization to the signal (we directly measure the power of this tone with a power meter). This tone can now be used to determine the total homodyne efficiency by measuring its power on the spectrum analyzer, taking the other losses into account. Our typical homodyne efficiency is $\eta_{\mathrm{HD}} = 66\%$ resulting in a total setup efficiency (detection efficiency of optical signal photons in the on-chip waveguide) of roughly $\eta_{\mathrm{Setup}} = \eta_{\mathrm{CP}} \cdot \eta_{23} \cdot \eta_{3\mathrm{H}} \cdot \eta_{\mathrm{HD}} \approx 48\%$.

B. Data collection procedure

Careful calibration of our data is crucial in understanding all noise sources and potential drifts over time in our setup. The losses in our setup are determined before we make a new data run as described in the previous section. We then proceed to record an optical trace of the cavity resonance by switching the light to a photodetector (PD1 in figure S2) and scanning the laser wavelength. This trace provides the information to lock the laser to a fixed detuning (typically $0.04 \cdot \kappa$ red of the cavity resonance), which is accomplished using a simple software lock and feedback from the wavemeter (with a resolution of roughly $0.003 \cdot \kappa$) and is described in more detail in the subsection below. As a next step the optical signal is switched to the homodyne detector and the relative phase between the signal and the local oscillator is scanned using the fiber stretcher in the LO arm. The resulting interference is shown in figure S3 as the blue trace. The interference signal is used to lock the relative phase between the signal and LO using a Toptica DigiLock 110. The green traces show the properly locked signal, while the red traces are phase set points where the lock failed requiring the associated data to be discarded. We then record the spectra of the homodyne signal and for every trace taken we also save a spectrum of the shot-noise by switching the signal arm away from the homodyne detector and only measure vacuum input to the signal arm of our detector. We re-lock the laser with respect to the cavity every other data point to counteract drift. This procedure is repeated for several different phases and different input powers. We typically took data for 60 different phases for every input power within a range of a little less than $-\pi/2$ to $\pi/2$.

C. Relation between detuning and quadrature

The laser frequency is positioned at a detuning of roughly $0.04 \cdot \kappa$ by starting at a larger detuning on the red side of the cavity, and stepping the laser blue in 0.1 pm steps (12 MHz) towards the cavity while monitoring the

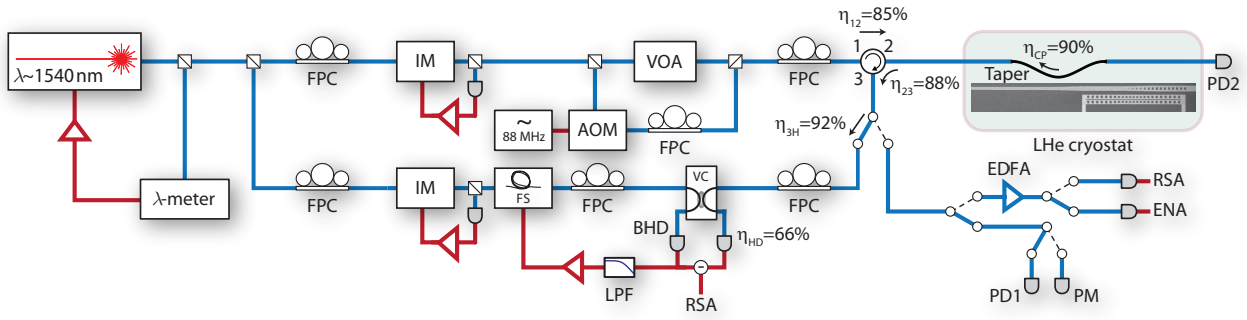

FIG. S2. **Experimental setup.** A detailed description of the experimental setup can be found in the main text.

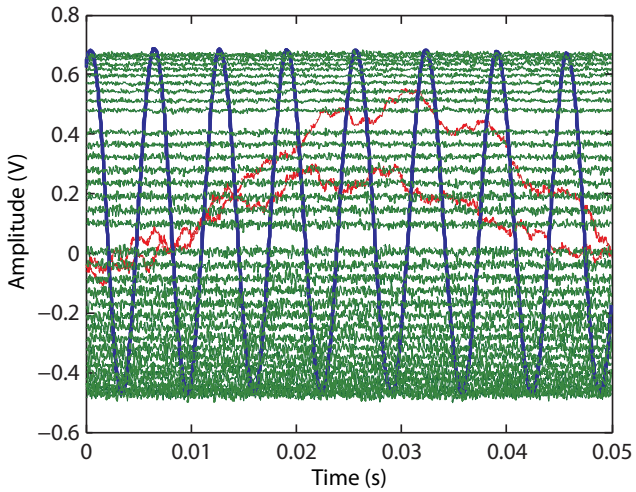

FIG. S3. **Phase information.** The blue trace shows the interference signal of the local oscillator and the signal on the homodyne detector when their relative phase is scanned using a fiber stretcher in the local oscillator (LO) arm. The voltage reading here is proportional to $\cos(\theta - \phi)$ where θ is the phase difference between the LO and input to the cavity, and ϕ is the phase imparted by reflection off the cavity. This interference signal is used to actively stabilize the relative phase to different set points (green traces). Occasionally the lock fails, as shown by the red traces, and any associated data is discarded. The range in which the phase can be stably locked is slightly smaller than $-\pi/2$ to $\pi/2$ due to the turning points in the sinusoidal interference curve.

average intensity of the reflected light on PD1. Once the target intensity is reached, the laser is kept at this wavelength during the course of the measurement by the wavemeter lock without further feedback from PD1. The intensity reading gives us an idea of the value of the detuning which is determined more accurately by analysis of our homodyne spectra.

The homodyne spectra are taken at different phase lock points (see Fig. S3) corresponding to quadrature angles $\theta_{\rm lock}$ between the reflected signal and the LO. These angles differ from our convention in Section I where the phase θ between the *input* light into the cavity and the local oscillator is considered. They are related to one another by the phase imparted on the input light upon reflection from the cavity,

$$\phi(\Delta) = \mathrm{Arg}\left[1 - \frac{\kappa_e}{i\Delta + \kappa/2}\right], \tag{S29}$$

and the relation

$$\theta_{\rm lock} = \theta - \phi. \tag{S30}$$

For a given laser-cavity detuning Δ, we sweep through the different phase lock points (see Fig. S3) $\theta_{\rm lock}$, and take mechanical spectra for each phase. The phase that minimizes the mechanical signal $\theta^*_{\rm lock}$ is determined from the recorded spectra. This allows us to solve for Δ using the expression $\theta^*_{\rm lock} = \theta^*(\Delta) - \phi(\Delta)$ where $\theta^*(\Delta)$ is the phase minimizing the mechanical transduction according to the model in the previous section. To first order (for $\Delta \ll \kappa$) θ^* is 0 since no mechanical signal is observed in the intensity quadrature of the reflected light. This post-processing of the data allows us to determine that across the measured powers the detuning was $\Delta = 0.044 \cdot \kappa \pm 0.006 \cdot \kappa$. For a single measured power, we expect a more accurate determination, with an uncertainty on the order of $0.003 \cdot \kappa$. This level of accuracy in the detuning also determines the uncertainty in quadrature angle of 0.04 rad.

III. SAMPLE FABRICATION AND CHARACTERIZATION

A. Fabrication

The devices are fabricated from a silicon on insulator (SOI) wafer (SOITEC, 220 nm device layer, 3 μm buried oxide, device layer resistivity $4 - 20\ \Omega \cdot$ cm) using electron beam lithography and subsequent reactive ion etching (RIE/ICP) to form the structures. The buried oxide is then removed in hydrofluoric acid (49% aqueous HF solution) and the devices are cleaned in a piranha solution

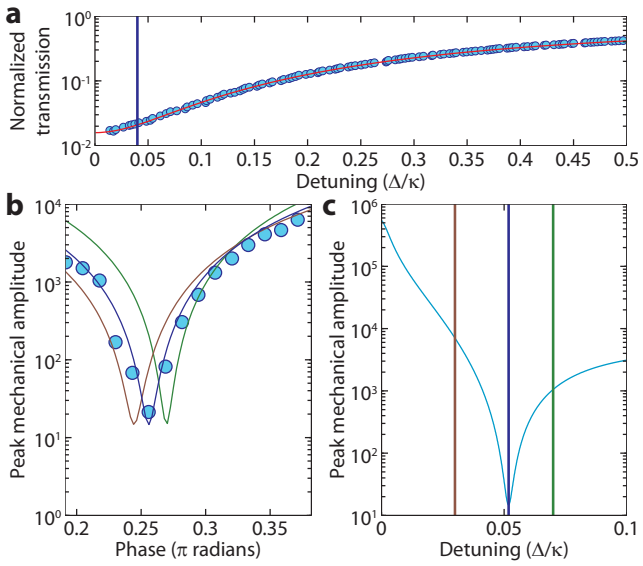

FIG. S4. **Detuning and phase lock points. a**, An optical scan taken before the data run starts is shown. The blue vertical line denotes the target detuning the software lock moves the laser to, determined from the measured reflection intensity. The laser is kept at that detuning via a wavemeter lock, as the light is switched away from PD1 and to the homodyne detector. The measured area under the mechanical mode is plotted in **b** (blue circles) at this detuning. A minimum value is reached for a local oscillator to reflected signal phase of $\theta^*_{\rm lock}$. Depending on the detuning, different mechanical mode amplitudes can be measured at this phase angle $\theta_{\rm lock}$, according to the model. We obtain an accurate estimate of the detuning by calculating the detuning at which the mechanical mode amplitude is minimized at the measured $\theta_{\rm lock}$ as shown in **c**. The expected mode amplitudes for the detunings represented by the red and green lines in **c** are shown by the similarly colored curves in **b**.

(3:1 H_2SO_4 and H_2O_2) and finally hydrogen terminated in diluted HF. For a more detailed description see [15].

B. Optical Characterization

The optical characterization of our devices is done by sweeping the laser frequency across the optical resonance while detecting the reflected light in a photodetector (PD1 in figure S2). This light is simultaneously sent to a wavemeter to record the absolute wavelength and accurately determine the linewidth and center frequency of the resonance. Each chip contained several designs where the waveguide loading (coupling) of the optical cavity was varied by changing the gap size between the waveguide and nanobeam. For our measurements we chose a slightly overcoupled ($\kappa_e/\kappa_i \approx 1.22 > 1$) device with good optical quality (57,000 loaded Q) [16].

C. Mechanical Characterization

The intrinsic mechanical damping rate γ_i and the optomechanical coupling rate g_0 are measured by detecting the mechanical response to the signal laser, through the reflected signal field, on the spectrum analyzer. We keep the optical power constant, while we take measurements for several different detunings Δ. The radiation pressure force causes both an optical spring effect resulting in a frequency shift of the mechanical resonance, as well as damping of the mechanical motion, associated with a broadening of its linewidth (see equations (S4) and (S5)). By fitting the data shown in figures S5a and S5b, we can extract $\gamma_i = 2\pi\times172$ Hz and $g_0 = 2\pi\times750$ kHz. Knowing the mechanical properties of our resonator and the precise intracavity photon number, we can now also extract the mechanical bath occupancy n_b as a function of detuning from the measured PSDs of the mechanical mode (figure S5c; see also [17]). This shows us that our mechanical mode thermalizes to about 16 K for low optical input powers, which is close to the cold finger temperature of our cryostat of 10 K.

D. Mechanical quality factor measurements

During our experiments, we observed a change in the Q-factor of the mechanical resonances of the zipper cavity devices after initial cool down. We believe this behavior is due to the unpassivated surface of the silicon nanomechanical resonator, and the adsorption of contaminents on the silicon surface during temperature cycling of the sample. Early on in each experimental run, the mechanical resonators exhibit mechanical quality factors of $Q_m \sim 10^6$. Figure S6 shows the auto-correlation of the thermal Brownian motion [18] of the fundamental in-plane differential mode of the zipper cavity device studied in the main text prior to temperature cycling of the sample, indicating a correlation time of 4 ms corresponding to a mechanical Q-factor of $Q_m = 7\times10^5$. Following temperature cycling, this large mechanical quality factor deteriorates to the reported $Q_m \approx 1.6\times10^5$ in the main text of the manuscript. Following the first temperature cycling, the mechanical Q-factor is stable at this reduced value for the remainder of the cool-down (roughly a week). Passivation of the silicon surface (i.e., through a thin oxide), should allow the mechanical Q to be stable at the initially measured high Q values.

Assuming an increase of the decoupling from the thermal bath of approximately an order of magnitude, and assuming that this decoupling is uniform across all the modes of the structure, maximum squeezing of 22% below shot-noise can be achieved at the demonstrated detection efficiency. This corresponds to 45% (2.6 dB) squeezing of the reflected light below shot-noise in the silicon waveguide for the cavity-coupling demonstrated in this work, and around 85% (8 dB) squeezing below

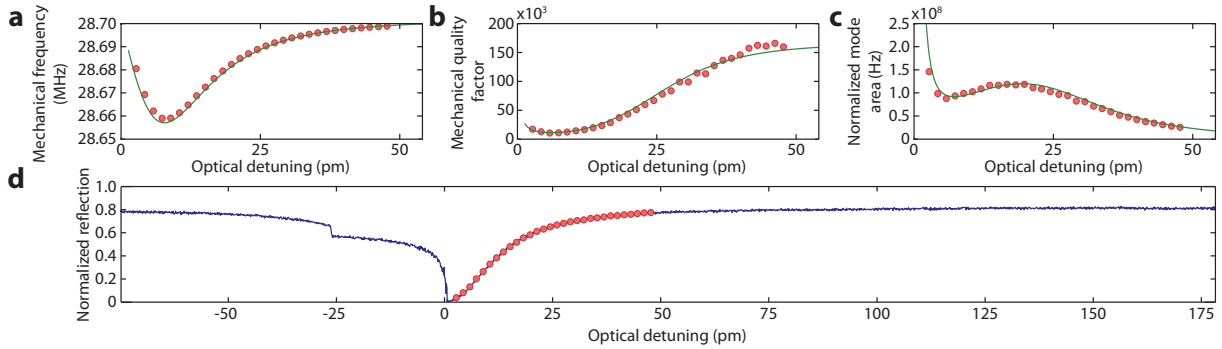

FIG. S5. **Optomechanical characterization.** We characterize the behavior of the optomechanical system in order to extract several parameters such as the intrinsic mechanical linewidth $\gamma_{\rm i}$, the optomechanical coupling rate g_0, and the bath temperature $T_{\rm b}$ ($n_{\rm b}$). **a**, The effective mechanical frequency $\omega_{\rm m} = \omega_{\rm m0} + \delta\omega$ described in equation (S4) is plotted as a function of the laser detuning $\Delta = \omega_{\rm o} - \omega_{\rm L}$ (shown here in units of wavelength). The frequency shift is due to the optical spring effect caused by radiation pressure. **b**, The optomechanical interaction also causes the intrinsic linewidth $\gamma_{\rm i}$ of the mechanical mode to be broadened as the detuning is changed (cf. equation (S5)). **c**, The area under the mechanical Lorentzian is also modified depending on Δ, and is shown here, normalized to shot-noise. The fits (green lines) in **a**–**c** are now used to obtain $\gamma_{\rm i}$, g_0 and $n_{\rm b}$ (see text for details). The plot in **d** shows a normalized cavity scan, which is used to determine the exact detunings in **a**–**c**, with every red data point corresponding to a data point in **a**, **b** and **c**.

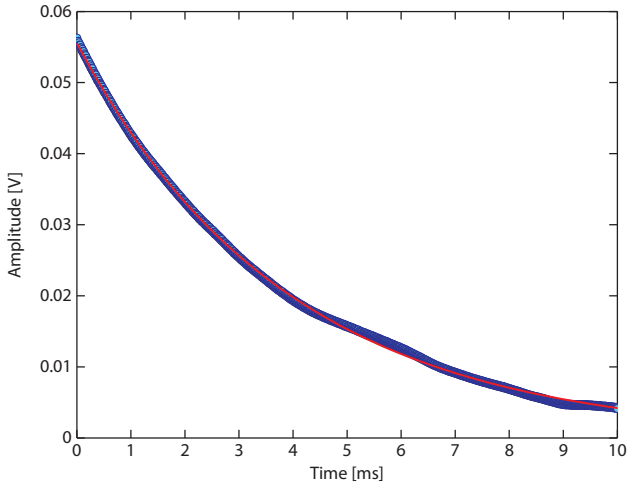

FIG. S6. **Mechanical Q-factor prior to thermal cycling.** Shown is the auto-correlation function of the position fluctuations squared for the fundamental in-plane differential mechanical motion of the zipper cavity prior to thermal cycling. The plot shows that the device initially exhibits a coherence time of 4 ms corresponding to a mechanical quality factor of 7×10^5.

shot-noise with optimal cavity-coupling ($\kappa = \kappa_e$).

IV. NOISE SPECTROSCOPY DETAILS

A. Homodyne measurement with laser noise

Our experiment is designed to measure the spectral density of the fluctuations of the optical field exiting the cavity. However, any real laser system will have technical noise, in addition to the quantum noise associated with an ideal coherent source, which adds to the detected noise level. Both the signal and local oscillator arm of our setup contain this noise which must be taken into account. The noise on the signal arm can also be modified non-trivially by propagation through the optomechanical system. We start by reproducing known results on the operation of an ideal, balanced homodyne detection system with signal and local oscillator input fields $\hat{a}_{\rm s}$ and $\hat{a}_{\rm LO}$ respectively, under the influence of noise [19–21]. Most generally, these fields consist of coherent tones $\alpha_{\rm s}$ and $\alpha_{\rm LO}$, technical (or classical) noise components $a_{\rm s,N}(t)$ and $a_{\rm LO,N}(t)$, and quantum fluctuations $\hat{a}_{\rm s,vac}(t)$ and $\hat{a}_{\rm LO,vac}(t)$:

$$\hat{a}_{\rm s} = \alpha_{\rm s} + a_{\rm s,N}(t) + \hat{a}_{\rm s,vac}(t), \tag{S31}$$

$$\hat{a}_{\rm LO} = \alpha_{\rm LO} + a_{\rm LO,N}(t) + \hat{a}_{\rm LO,vac}(t). \tag{S32}$$

Since both the local oscillator field and the signal field are generated by the same laser, the technical noise on the signal and local oscillator will be correlated, and these correlations must be accounted for in the analysis. For the simplest case, where the signal arm does not experience the complex dispersion from interaction with an optomechanical system (e.g. being reflected off the end-mirror far detuned from the optical resonator), we expect

$$a_{\rm s,N}(t) = \alpha_{\rm s}\xi(t) \quad \text{and} \quad a_{\rm LO,N}(t) = \alpha_{\rm LO}\xi(t). \tag{S33}$$

The function $\xi(t)$ is related to the intensity and phase fluctuations of the laser light ($n(t)$ and $\phi(t)$ respectively):

$$a(t) = a_0(1+n(t))e^{i\phi(t)} \approx a_0(1+n(t)+i\phi(t)),$$
$$\xi(t) = n(t) + i\phi(t). \quad \text{(S34)}$$

The difference of the photocurrent in the homodyne detector is given by

$$\hat{I}(t) = \hat{a}_s\hat{a}_{LO}^\dagger + \hat{a}_s^\dagger\hat{a}_{LO}, \quad \text{(S35)}$$

which, considering only the technical noise, reduces to

$$\hat{I}(t) = |\alpha_{LO}|\hat{X}_\theta^{(s,vac)} + I_{DC}(1+2\mathrm{Re}\{\xi(t)\}), \quad \text{(S36)}$$

under the assumption that $\alpha_{LO} \gg \alpha_s$, using the definitions in equation (S33), and taking the DC current $I_{DC} = 2\mathrm{Re}\{\alpha_s^*\alpha_{LO}\} = 2|\alpha_s\alpha_{LO}|\cos(\theta)$, where θ is the relative phase between the signal and local oscillator. From this equation we see that the phase noise $\phi(t)$ cannot be detected on a balanced homodyne setup. This can be understood as being from the detectors fundamental insensitivity to phase noise on the laser, as the only phase reference in the system is the local oscillator, which contains the same phase fluctuations as the signal. Secondly, for the local oscillator phase which makes $I_{DC} = 0$, intensity noise is not detected. In a real homodyne detector this is only true for a perfect common mode rejection ratio (CMRR), which is the case in our setup as the intensity noise is negligible and the CMRR is > 25 dB. For these reasons we use a different setup for characterizing the laser phase and intensity noise as described in Section IV B.

B. Measurement and characterization of laser noise

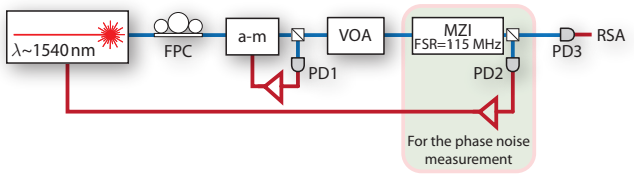

FIG. S7. **Experimental setup for characterization of intensity and phase noise.** The laser is amplitude stabilized and an attenuator is used to select the desired optical power. For the phase noise measurement the light is sent through a Mach-Zehnder interferometer (MZI) with a free spectral range of 115 MHz. The laser is locked to the center of the interference fringe allowing frequency noise to be converted to intensity noise. The light is then detected on a New Focus Model 1811 photodetector and the photocurrent detected on a spectrum analyzer. The same setup is used to detect intensity noise without the MZI.

In this section we discuss the procedure used for characterization of our laser (New Focus TLB-6728-P-D). This characterization was done using an independent setup, shown in figure S7, and involved two measurements directly detecting the light.

The first measurement is to characterize the intensity noise where the laser light is sent directly onto a photodetector with the incident power varied. From the theory we expect for the detector photocurrent

$$I(t) = (\alpha_{LO} + a_{LO,N}(t) + \hat{a}_{LO,vac}(t))^\dagger(\text{h.c.})$$
$$= |\alpha_{LO}|\hat{X}_{\theta=0}^{(LO,vac)} + I_{DC}(1+2\mathrm{Re}\{\xi(t)\}), \quad \text{(S37)}$$
$$\text{with} \quad I_{DC} = |\alpha_{LO}|^2.$$

The spectral density of the current is then given by

$$S_{II}(\omega) = |\alpha_{LO}|^2\left(1 + |\alpha_{LO}|^2 S_{nn}(\omega)\right), \quad \text{(S38)}$$

where $S_{nn}(\omega)$ is the PSD of the intensity noise fluctuations. For a real detector, this equation is modified by the presence of a dark current $S_{dark}(\omega)$ and non-unity efficiency ($\eta_{det} < 1$):

$$S_{II}(\omega) = S_{dark}(\omega) + |\alpha_{LO}|^2\left(1 + \eta_{det}|\alpha_{LO}|^2 S_{nn}(\omega)\right). \quad \text{(S39)}$$

We subtract the dark current (measured with the laser turned off) from the data, and set bounds on the magnitude of the intensity noise present in the laser by examining the linear and quadratic dependence of the noise floor with respect to power. The linear component is due to shot-noise, while the quadratic variance is due to the intensity noise fluctuations (see equation (S39)). The results are shown in figure S8a and c. The noise floor was seen to only increase linearly with laser power, confirming the absence of intensity noise at the frequencies of interest.

A second measurement is done to characterize the phase noise properties of the system. By sending the laser through a Mach-Zehnder interferometer (MZI) with transfer function $I(t) = I_0(1+\sin(2\pi\omega/\omega_{FSR}))$, the intensity of the transmitted light will contain fluctuations related to the frequency fluctuations of the light (see figure S8). The free spectral range (FSR) of the MZI is $\omega_{FSR}/2\pi = 115$ MHz. For a real detector, and assuming $\omega \ll \omega_{FSR}$, we arrive at

$$S_{II}(\omega) = S_{dark}(\omega) + |\alpha_{LO}|^2\left(1 + \eta_{det}\frac{|\alpha_{LO}|^2}{\omega_{FSR}^2}S_{\phi\phi}(\omega)\right).$$

Some phase noise was detected, as shown in figure S8b and d and the quadratic dependence of the PSD on signal power. The spectral densities show a roll-off due to the FSR of the MZI. It was found that in the frequency range of interest, 1 MHz $< \omega/2\pi <$ 40 MHz, the frequency noise spectral density, $S_{\omega\omega}(\omega) = \omega^2 S_{\phi\phi}(\omega)$, is flat, and roughly equal to $3-6\times10^3$ rad$^2\cdot$Hz, in agreement with previous characterization of the same laser at higher frequencies [13].

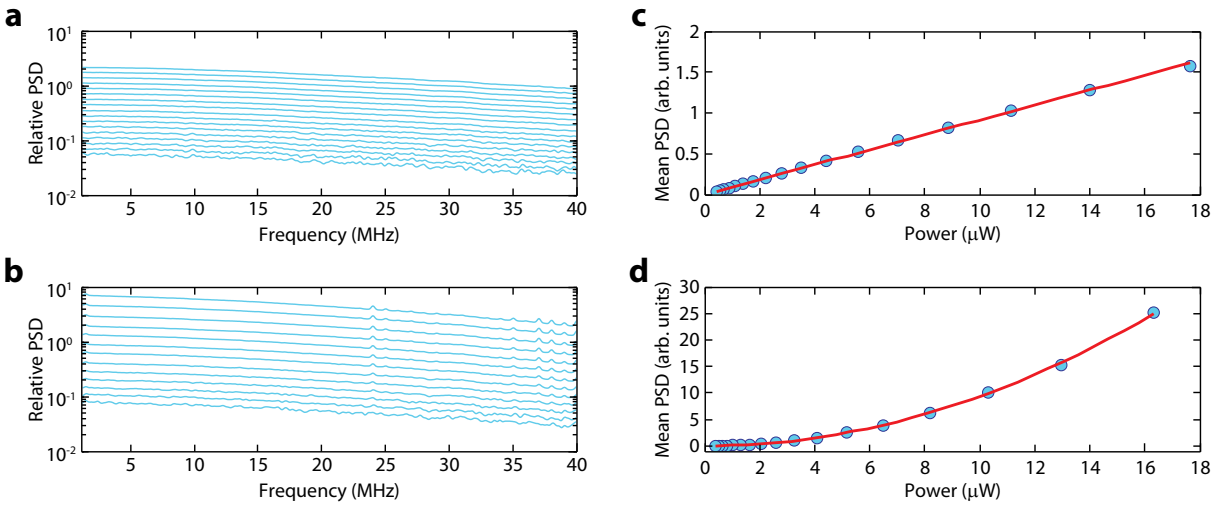

FIG. S8. **Laser noise characterization.** **a**, We measure the power spectral density (PSD) of our laser for several powers, normalize to and then subtract it from the dark current of the detector. The same measurement is performed using a Mach-Zehnder interferometer locked at half of the fringe amplitude in order to convert any frequency noise to intensity noise to allow detection and is shown in **b**. **c**, Plot of the mean value of the PSD around the mechanical frequency ω_{m} from the measurement done in **a** as a function of power. The good linear fit (red line) indicates that no intensity noise is present. **d**, Mean PSD of the measurement in **b**. The quadratic fit (red line) shows that phase noise is indeed present (see text for more details).

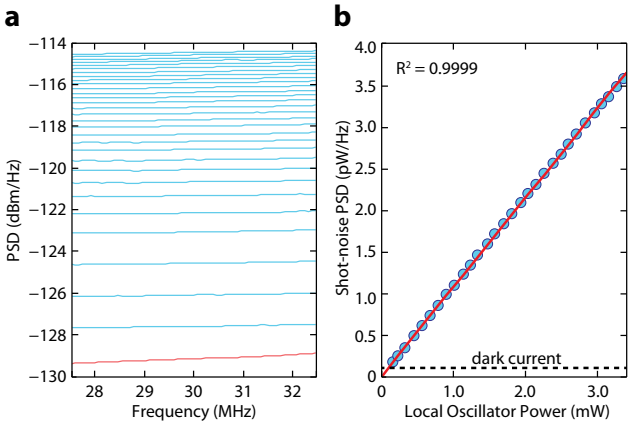

FIG. S9. **Noise level versus power.** **a**, Electronic noise power spectral densities from the balanced homodyne detector at different local oscillator powers (under a balanced condition). The red trace corresponds to the electronic noise floor with zero local oscillator power, i.e. the dark current. **b**, Mean value of the power spectral densities shown in **a** as a function of local oscillator power. In this plot the electronic noise or dark current contribution (0.12 pW/Hz, shown by the dashed black line) is subtracted. The red line is a linear fit, which has a coefficient of determination $R^2 = 0.9999$. The local oscillator power used in the experiment presented in the main text corresponds to 3.0 mW.

C. Linearity of detector with local oscillator power

Having characterized the laser with an independent setup, we try to understand the properties of the measurement system. Our first measurement is designed to characterize the linearity of the detector and amplifier. With $I_{\mathrm{DC}} = 0$, and no signal in the signal arm of the BHD, we expect the system to faithfully reproduce the relation (S36) showing a linear relationship between local oscillator power and the detected signal vacuum fluctuation (shot-noise) noise level. It is observed that the mean values of the PSDs linearly depend on the input power as expected and shown in figure S9. This indicates that our detector (and its amplifier) are in fact linear. The red line is a linear fit, with a coefficient of determination of $R^2 = 0.9999$. Although we already confirmed that no measurable amount of intensity noise is present (cf. figure S8), in the case we would have an appreciable amount of noise this measurement would show that it is smaller than the CMRR.

D. Detected noise level with unbalancing

A second measurement with vacuum input on the signal is done to understand how the amplifier in the homodyne detector depends on the DC level of the electronic signal after the photocurrent is subtracted. Here we use the variable coupler to change the splitting ratio and cause an imbalance between the optical power levels in the arms. The detected noise floors are shown in

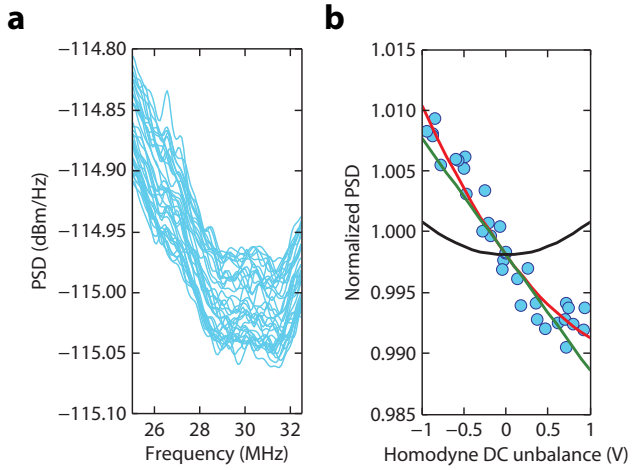

FIG. S10. **Amplifier gain.** **a**, Shown are the power spectral densities (PSDs) of the local oscillator as a function of the balancing of the optical power in the two paths of the homodyne detector. Each trace represents a different ratio of power in each path. These traces were taken with a local oscillator power of 3.0 mW, as used in the experiment. **b**, The mean value of the PSDs normalized to the perfectly balanced PSD are shown as a function of the difference voltage on the two photodiodes in the homodyne detector, where zero voltage represents perfect balancing. The green line is a linear fit to the data, while the black curve is a quadratic model, which describes any classical intensity noise that could cause the difference in the level of the PSDs. The red curve is the sum of the two. The change in PSD with homodyne unbalancing can be fully explained by the small signal gain weakly dependent on the detector unbalancing (linear fit) and no classical intensity noise (as previously determined).

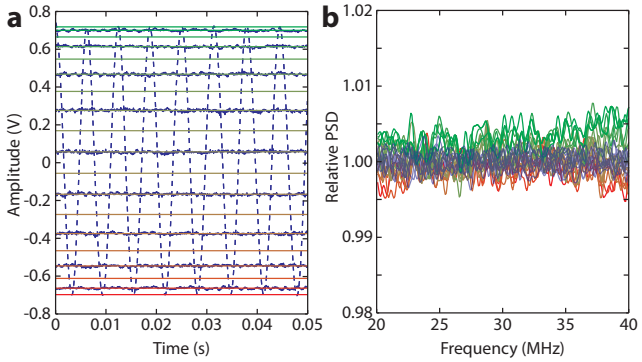

FIG. S11. **Detuned noise.** The laser is detuned with respect to the cavity resonance by 1 nm and spectra are taken using the homodyne detector over a range of phase angles, with a local oscillator power of 3.0 mW. This lets us estimate the amount of additional intensity noise we might acquire in our optical signal train. **a**, The dotted blue line shows the amplitude of the interference of the signal and local oscillator as a function of time. We lock at several relative phases (color-coded from green to red in **a** and **b**) and plot the associated normalized power spectral densities (PSD) relative to shot-noise in **b**. For every second measurement we switch the signal beam off to obtain the shot-noise level (blue traces). The maximum difference in the noise level is around 0.5%.

figure S10a, and the mean detected PSDs are shown in figure S10b, normalized to the shot-noise level. We find that at larger $V_{\rm DC}$ (linearly related to $I_{\rm DC}$), there is a very small ($< 2\%$) drop in the gain of the detector. Using a linear fit, we extract an adjustment to the gain vs. output DC current. This means that for a measured noise power spectral density $S_{\rm meas}(\omega)$ taken at a DC voltage $V_{\rm DC}$, we estimate that the actual PSD, compensating for modified gain, is $S(\omega) = (1+V_{\rm DC}/(-0.0096))^{-1} S_{\rm meas}(\omega)$. This modification is used from here on, and only reduces the amount of squeezing we observe, as the quadratures with squeezing are always at positive voltages. Additionally, the largest DC voltages we work at are roughly ± 1 V, which results in a modification on the order of one percent.

E. Estimating added noise in the optical train

In our third measurement, we reflect the laser light off the end mirror of the waveguide coupler (detuned by 1 nm from the cavity), and measure the detected noise level as a function of θ, the phase difference between local oscillator and signal. This measurement is sensitive to both the conversion of phase noise to intensity noise through dispersion in the optical train, and added noise due to additional noise processes in the optical train such as guided acoustic-wave Brillouin scattering (GAWBS) [22], which could cause uncorrelated noise in the local oscillator and signal arms (see Eq. (S36)). The results of this measurement are shown in figure S11a and b. The first figure shows the DC interference signal between the local oscillator and signal used in the measurement. The LO power used for this experiment was the same as for the actual squeezing data, and the signal level used is on the same order as used for the highest power measurements, as is evident from the swing of about 1.4 V in the DC interference signal. The highest DC swing observed in the experiment was 1.6 V. The second figure shows the normalized (to shot-noise) power spectral density where an increase of at most 0.5% is observed, indicating these sources of noise do not contribute in our experiment.

F. The effect of laser phase noise

Using the measured value for the spectral density of phase and frequency fluctuations from section IV B, the effect of laser technical noise on the detected squeezing spectra can be calculated. Following the derivation in section I C and taking the classical noise component of the field input to the cavity to be $a_{\rm in}^{(\rm N)}(\omega) = i\alpha_{\rm in}\phi(\omega)$

(with a corresponding LO phase noise of $a_{\rm LO}^{(\rm N)}(\omega) = i\alpha_{\rm LO}\phi(\omega)$), we arrive at an expression for the output noise due to input phase noise from the cavity:

$$a_{\rm out}^{(\rm N)}(\omega) = i\alpha_{\rm in}(1 + A_1(\omega) - A_2(\omega))\phi(\omega). \quad \text{(S40)}$$

Without optomechanical interaction ($G = 0$) we find $A_1(\omega) = -\kappa/(i(\Delta - \omega) + \kappa/2)$, and $A_2(\omega) = 0$. We calculate the expression for the current noise due to laser phase noise using this expression:

$$\begin{aligned} I^{(\rm N)}(\omega) &= \alpha_{\rm LO}^* a_{\rm out}^{(\rm N)}(\omega) + \alpha_{\rm LO}[a_{\rm out}^{(\rm N)}(-\omega)]^* \\ &\quad + \alpha_{\rm out}^* a_{\rm LO}^{(\rm N)}(\omega) + \alpha_{\rm out}[a_{\rm LO}^{(\rm N)}(-\omega)]^* \\ &= F(\omega)\phi(\omega) \end{aligned} \quad \text{(S41)}$$

with $F(\omega) = i|\alpha_{\rm LO}\alpha_{\rm in}|[e^{-i\theta}(r(\omega) - r(0)) + e^{i\theta}(r(-\omega) - r(0))^*]$, where $r(\omega)$ is the amplitude reflection coefficient of the cavity. The PSD of the photocurrent due to phase noise is found to be

$$S_{II}^{(\rm N)}(\omega) = |F(\omega)|^2 S_{\phi\phi}(\omega). \quad \text{(S42)}$$

For a system with no dispersion, $r(\omega) = $ const., it can be easily shown that $F(\omega) = 0$ as expected. For an overcoupled cavity with no optomechanical coupling, $r(\omega) = 1 - \kappa/(i(\Delta - \omega) + \kappa/2)$, so $r(\omega) - r(0) \approx 4i\omega/\kappa$, and we have $F(\omega) = 8i|\alpha_{\rm LO}\alpha_{\rm in}|\sin(\theta)(\omega/\kappa)$. The ω dependence of $F(\omega)$ means that a flat frequency fluctuation spectrum ($S_{\phi\phi} \propto \omega^{-2}$, as we observe) adds a flat noise floor to the detected signal.

Finally we note that phase noise on the laser can drive the mechanical motion and cause heating. This effect is negligible since we are tuned near resonance, where only the intensity fluctuations affect the mechanics, and our cavity has a very large linewidth κ.

G. Error Analysis

The estimates of uncertainty in the squeezing values reported could mainly come from three sources. First, the detector may be nonlinear. Our characterization of the detector, and the presented calibration data in Figure S9 rule this out as a significant source of error ($\ll 0.1\%$). Secondly, the gain of the detector shows some dependence on the lock-point (with a maximum change on the order of $\pm 1\%$), which we characterize and factor out, as explained in section IV D. This compensation of the systematic error has some statistical uncertainty associated with it, and we estimate this to be about $\pm 0.1\%$. Finally, there are statistical fluctuations in the detected noise level. We characterize these by looking at the variance of the detected shot-noise levels over a large bandwidth, and find that the standard deviation of the detected noise power spectral density is about $\pm 0.15\%$ of the shot noise level. Summing in quadrature these sources of error, we estimate the uncertainty in our spectra to be on the order of $\pm 0.2\%$ of shot-noise.

H. Phenomenological dispersive noise model: the effect of structural damping

Mechanical damping of resonators and the associated fluctuations from coupling to the thermal bath has long been considered as an impediment to measuring weak forces in gravitational wave detectors [5, 6, 23–25]. In these studies the effect of the bath has often been encapsulated in a parameter $\Psi(\omega)$, representing the lag angle in the response of the material to a force. This lag angle is the complex part of the spring constant: $F = -k(1 + i\Psi(\omega))x$. The quality factor of the resonator is given by the narrow-band properties of the lag angle and its value at the mechanical resonance frequency, $Q = \Psi(\omega_{\rm m0})^{-1}$. We are interested in the wideband properties of $\Psi(\omega)$, since the spectral properties of the thermal fluctuations are related to the spectrum $\Psi(\omega)$, following the fluctuation-dissipation theorem.

In the case of our experiments, we observed noise floors for S_{xx} following a ω^{-1} power law on the low frequency end. This sort of noise power law corresponds to a flat spectrum for the lag angle $\Psi(\omega) = $ const. over the frequency range of interest. Unlike viscous damping which can be simply shown to have $\Psi(\omega) \propto \omega$ (since the force is proportional to velocity), a lag angle constant in frequency lacks a simple physical explanation, though it is ubiquitous in many types of mechanical resonators and commonly called "structural damping" [6].

In the input-output formalism outlined in section I we model this type of noise by taking the mechanical damping rate $\gamma_{\rm i}$ to be spectrally flat, and using frequency dependent bath correlation functions $\langle \hat{b}_{\rm in}(\omega)\hat{b}_{\rm in}^\dagger(\omega')\rangle = (\bar{n}(\omega) + 1)\delta(\omega + \omega')$, $\langle \hat{b}_{\rm in}^\dagger(\omega)\hat{b}_{\rm in}(\omega')\rangle = \bar{n}(\omega)\delta(\omega + \omega')$, $\langle \hat{b}_{\rm in}^\dagger(\omega)\hat{b}_{\rm in}^\dagger(\omega')\rangle = 0$, and $\langle \hat{b}_{\rm in}(\omega)\hat{b}_{\rm in}(\omega')\rangle = 0$. This constitutes our single-mode thermal noise model.

In any real optomechanical system, a family of mechanical modes couples to the optical resonance. In the modal picture which we use here, each of these mechanical resonances can be thought to add to the detected noise floor with its contribution scaling at the low-frequency end as ω^{-1}. The contribution of each mode is proportional to the bath temperature, $g_{0,\rm k}^2$, $\gamma_{\rm i,k}$, and $\omega_{\rm m,k}^{-2}$. We lump all of these contributions into a single effective mechanical resonance, with its properties (not all independently) determined by fitting to the low frequency end of the noise floor. This mechanical resonator is modeled with a mechanical frequency $\omega_{\rm m}/2\pi = 50$ MHz (so we operate in the low frequency tail), a mechanical quality factor $Q_{\rm m} = 100$, and a total coupling rate of $g_0/2\pi = 100$ kHz. We found that this model reproduced the magnitude and phase (the quadrature in which the noise is detected) of the ω^{-1} noise well, if an additional intracavity photon-dependent heating of $c_0 = 3.2 \times 10^{-4}$ K/photons is assumed. These background noise floors are plotted in figure S12. This cavity heating rate leads to the effective bath temperature to nearly double at the highest input powers, going from 16 K to over 30 K. This amount of

heating is in line with what we expect from thin-film photonic crystals we have fabricated in the past operating in the same cryostat [17].

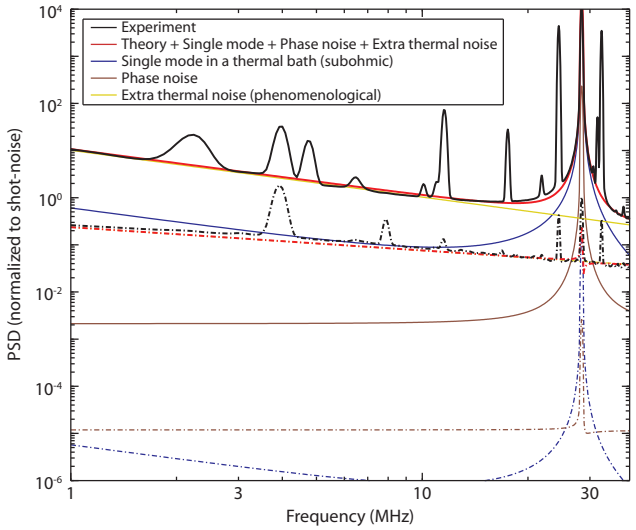

FIG. S12. **Noise model and experimental results.** The complete noise model, and constituent components, are plotted and compared to the experimental, shot-noise-subtracted power spectral density (PSD) for a quadrature sensitive to the mechanical motion (solid curves) and an insensitive quadrature (dotted dashed curves). The black lines are the experimental PSDs. The red lines represent the full noise model including contributions from a single mechanical mode (blue line), phase noise of the laser (brown line), and the extra thermal noise (yellow line) as described in section IV H. The deviation between the modeled and experimental data predominantly results from additional mechanical modes.

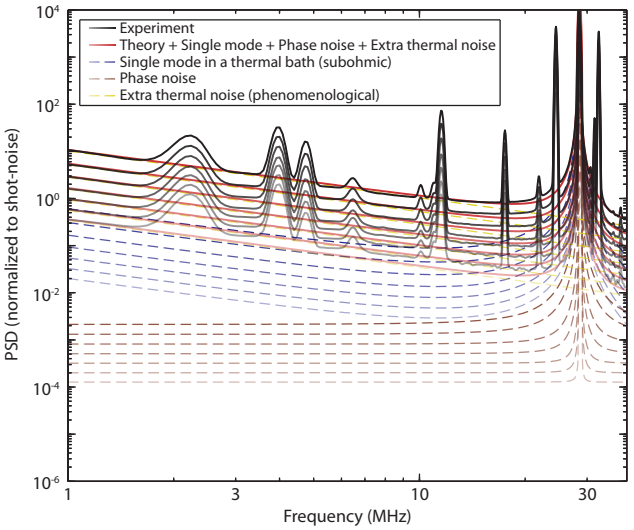

FIG. S13. **Power spectral densities (PSD) of noise contributions with varying powers.** The complete noise model along with its constituent components and experimental data are shown for varying optical powers. The shot-noise has been subtracted from all curves. The experimental data are shown in black with the full noise model in red consisting of the single mechanical mode (dashed blue), phase noise (dashed brown), and extra thermal noise (dashed yellow). The optical power scaling is represented by the transparency of the individual curves with curves becoming less transparent with increasing optical power. The traces from highest power to lowest power correspond to intracavity photon numbers of $n_c = 3140$, 1990, 1250, 792, 498, 314, and 196 photons (2 dB steps).

I. Phenomenological absorptive noise model

In addition to the noise in the quadrature of the mechanical motion (which arises from fluctuations in the cavity frequency ω_o, and we suspect is mechanical in origin), we observed a significant amount of noise in the opposite quadrature, which can be interpreted to arise from fluctuations of the cavity decay rate κ. Additionally, we observed a different noise floor power law ($\omega^{-1/2}$) for this noise, which may rule out an optomechanical origin. The power law scaling agreed with thermorefractive noise studied extensively in the context of gravitational wave detection [24], microspheres [26], and microtoroids [27], but it is expected that thermorefractive coupling is predominantly in the same quadrature as the mechanical noise, which is not observed here. Also, if thermorefractive, the noise should show strong variation with temperature through both a quadratic temperature scaling (T^2) and an extremely steep variation of dn/dT in the temperature range of 16 K to 30 K [28], which was not observed. At this point, we have no noise model to explain the observed fluctuations, and the origin of this noise will be the subject of further investigation to be presented at a later time. A phenomenological noise model was instead used, where fluctuations in the cavity linewidth proportional to the intracavity power with a $\omega^{-1/2}$ noise spectrum are assumed.

J. Comparing measured spectra to theoretically predicted spectra

Our spectrum analyzer (Tektronix RSA3408B) operates by taking Fourier transforms of a time domain signal. By windowing a short time sample, and calculating its energy spectrum, a power spectral density is constructed. The size of the window in the time-domain affects the resolution bandwidth, and is well known in signal processing, multiplication by a Gaussian window of length τ is equivalent to convolution of the frequency domain signal by a Gaussian with width proportional to τ^{-1}. All of the measured data, except that presented in section III C was taken with a 40 MHz window and 300 kHz resolution

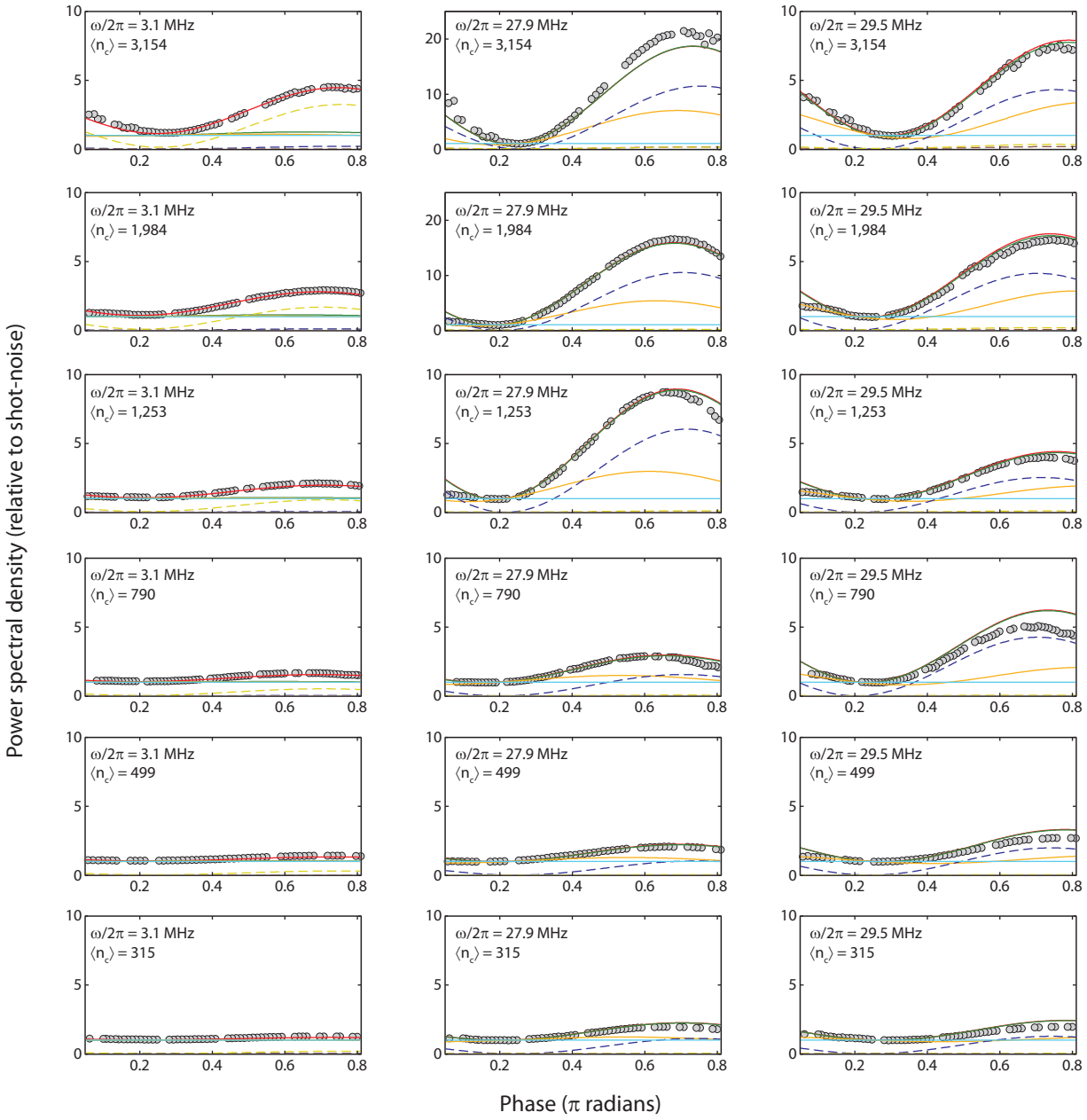

FIG. S14. **Detected noise power at a given frequency vs. the lock angle.** In these plots, a series of traces is shown of the detected noise level at a given frequency (with resolution bandwidth of 300 kHz) as a function of the locked phase θ_{lock}. The grey points are the measured data points. The solid lines are the results of the models detailed in the text, and the dashed lines represent the different components of noise present in each model. The red line shows the full noise model, containing the transduced thermal brownian motion from the studied mode, the noise due to structural damping present in the system, the phase noise, and the phenomenological out-of-quadrature noise. The green line is for a model considering all the same noise contributions, except the phenomenological component. A model considering a system without any thermal noise is shown in orange. With no thermal force on the mechanical systems, the detected signal in this case can be attributed to radiation pressure shot-noise heating. The shot-noise level is denoted by a light blue line. The contribution due to thermal motion of the mode of interest is shown by the dashed blue line. The noise contributions due to phase noise and structural damping are much smaller and shown by the brown and yellow dashed lines, respectively.

bandwidth. The spectra contain 501 points spaced by 80 kHz in the frequency domain. Additionally, for a few

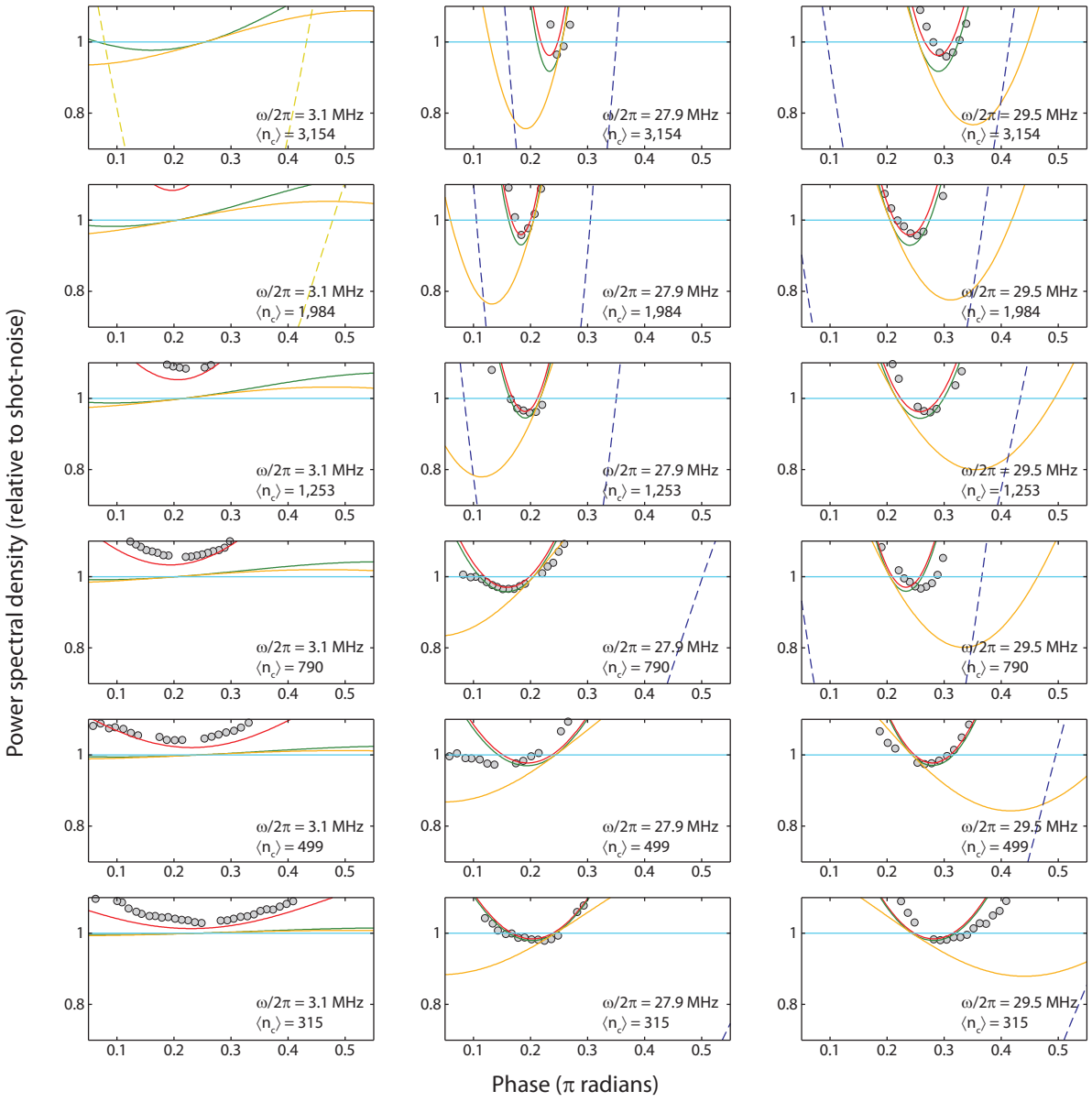

FIG. S15. **Close-up of detected noise power at a given frequency vs. the lock angle.** This close-up shows regions of squeezing, and the colors are the same as in Figure S14.

data sets we took narrow band spectra (down to 100 Hz resolution bandwidth) and found that the results agreed over the regions where squeezing was observed. The theory was calculated at 100 times finer resolution than the sampled data (with 50,000 points), and was then downsampled after a Gaussian convolution step simulating the operation of the spectrum analyzer. This only affects the size of the mechanical peak, and has no effect on the frequency ranges where we see sub-shot-noise fluctuation spectra. For the thermometry data in section III C, since we are interested in the mechanical linewidths and areas, the span was always chosen to be the minimum allowable by the RSA, which is twice as large as the linewidth.

V. SUMMARY OF NOISE MODEL

In Table I we present a summary of the parameters used in the theoretical model for the wideband squeezing spectra shown in the main text.

TABLE I. Model Parameters

Symbol	Name	Value	Measurement
Q_{optical}	Optical quality factor	5.7×10^4	Low-power optical spectroscopy with wavemeter. III B
η_κ	Cavity-waveguide coupling efficiency	0.55	Low-power optical spectroscopy with wavemeter. Verified phase response with ENA to distinguish from under-coupling. III B
$\gamma_i/2\pi$	Mechanical linewidth	172 Hz	Linewidth measurement vs. laser detuning in thermometry measurement (see section III C).
$g_0/2\pi$	Optomechanical coupling rate	750 kHz	Linewidth and mechanical frequency measurement vs. laser detuning in thermometry measurement (see section III C).
T_b^0	Bath temperature	16 K	Calibrated areas in thermometry measurement (see section III C).
c_0	Heating by optical absorption	3.2×10^{-4} K/photon	Rise of ω^{-1} noise floor with optical power (see section IV H). The cavity temperature according to this model rises from 16 K to roughly 30 K at the highest powers.
$S_{\omega\omega}$	Frequency noise spectral density	6×10^3 rad^{2}Hz	Frequency noise measurement with Mach-Zehnder Interferometer (see section IV B).
Δ	Laser detuning (red laser is positive)	$(0.044 \pm 0.006)\kappa$	The intensity of the reflected light is used to initially set the detuning. For a more accurate determination, the value of Δ minimizing the detected signal for the observed θ^*_{lock} is found (see Section II C).
θ_{lock}	lock angle	varies	The lock point (as in figure S3) is used to find the phase angle between the light reflected from the cavity and the local oscillator.
θ^*_{lock}	critical lock angle	varies	This is the lock angle where no mechanical signal is detected. It is found by looking at the area of the mechanical mode as a function of θ_{lock} (see Section II C).

VI. MATHEMATICAL DEFINITIONS

We present here the notational conventions used throughout this work for reference. The Fourier and inverse Fourier transforms of operator $\hat{A}(t)$ are defined as

$$\hat{A}(t) = \frac{1}{\sqrt{2\pi}} \int_{-\infty}^{\infty} d\omega \; e^{-i\omega t} \hat{A}(\omega) \quad \text{and}$$
$$\hat{A}(\omega) = \frac{1}{\sqrt{2\pi}} \int_{-\infty}^{\infty} dt \; e^{i\omega t} \hat{A}(t), \tag{S43}$$

respectively. The Hermitian conjugate of operator $\hat{A}(t)$ is given by $\hat{A}^\dagger(t)$ which has the Fourier transform $\hat{A}^\dagger(\omega)$. This is related to $\hat{A}(\omega)$

$$\left(\hat{A}(\omega)\right)^\dagger = \hat{A}^\dagger(-\omega). \tag{S44}$$

In the derivations presented here, we typically express a given operator in terms of the "input" bath operators. Expected values are then defined as $\langle\hat{A}(t)\rangle = \mathrm{Tr}[\rho_{\mathrm{in}}\hat{A}(t)]$, where ρ_{in} is the mixed state describing the bath. Spectral densities are found by taking the Fourier transform of the auto-correlation

$$S_{AA}(\omega) = \int_{-\infty}^{\infty} d\tau\ e^{i\omega\tau}\langle\hat{A}^\dagger(t+\tau)\hat{A}(t)\rangle. \tag{S45}$$

For a real operator, $S_{AA}(\omega) = S_{AA}(-\omega)$. For non-real operators, the spectral density can be symmetrized to $\bar{S}_{AA}(\omega)$:

$$\bar{S}_{AA}(\omega) = \frac{1}{2}(S_{AA}(\omega) + S_{AA}(-\omega)). \tag{S46}$$

These spectral densities can also be calculated from the frequency domain operators:

$$S_{AA}(\omega) = \int_{-\infty}^{\infty} d\omega'\ \langle\hat{A}^\dagger(\omega)\hat{A}(\omega')\rangle. \tag{S47}$$

We use the convention

$$\hat{X}_\theta^{(j)} = \hat{a}_j e^{-i\theta} + \hat{a}_j^\dagger e^{i\theta}. \tag{S48}$$

to define a measured quadrature of the field. This definition corresponds to having a phase difference of θ between input light and local oscillator.

[1] Gardiner, C. W. & Collett, M. J. Input and output in damped quantum systems: quantum stochastic differential equations and the master equation. *Phys. Rev. A* **31**, 3761–3774 (1985).

[2] Collett, M. J. & Gardiner, C. W. Squeezing of intracavity and traveling-wave light fields produced in parametric amplification. *Phys. Rev. A* **30**, 1386–1391 (1984).

[3] Gardiner, C. W. & Zoller, P. *Quantum Noise* (Springer Series in Synergetics, 2004).

[4] Clerk, A. A., Devoret, M. H., Girvin, S. M., Marquardt, F. & Schoelkopf, R. J. Introduction to quantum noise, measurement, and amplification. *Rev. Mod. Phys.* **82**, 1155–1208 (2010).

[5] Saulson, P. R. Thermal noise in mechanical experiments. *Phys. Rev. D* **42**, 2437 (1990).

[6] Gillespie, A. & Raab, F. Thermal noise in the test mass suspensions of a laser interferometer gravitational-wave detector prototype. *Phys. Lett. A* **178**, 357–363 (1993).

[7] Heidmann, A., Hadjar, Y. & Pinard, M. Quantum nondemolition measurement by optomechanical coupling. *Appl. Phys. B* **64**, 173–180 (1997).

[8] Verlot, P., Tavernarakis, A., Briant, T., Cohadon, P.-F. & Heidmann, A. Scheme to probe optomechanical correlations between two optical beams down to the quantum level. *Phys. Rev. Lett.* **102**, 103601 (2009).

[9] Børkje, K. *et al.* Observability of radiation-pressure shot noise in optomechanical systems. *Phys. Rev. A* **82**, 013818 (2010).

[10] Safavi-Naeini, A. H. *et al.* Observation of quantum motion of a nanomechanical resonator. *Phys. Rev. Lett.* **108**, 033602 (2012).

[11] Khalili, F. Y. *et al.* Quantum back-action in measurements of zero-point mechanical oscillations. *Phys. Rev. A* **86**, 033840 (2012).

[12] Jayich, A. M. *et al.* Cryogenic optomechanics with a Si_3N_4 membrane and classical laser noise. *New J. Phys.* **14**, 115018 (2012).

[13] Safavi-Naeini, A. H. *et al.* Laser noise in cavity-optomechanical cooling and thermometry. *New J. Phys.* **15**, 035007 (2013).

[14] Purdy, T. P., Peterson, R. W. & Regal, C. A. Observation of Radiation Pressure Shot Noise on a Macroscopic Object. *Science* **339**, 801–804 (2013).

[15] Chan, J. *Laser cooling of an optomechanical crystal resonator to its quantum ground state of motion.* Ph.D. thesis, California Institute of Technology (2012).

[16] Gröblacher, S. *et al.* in preparation. (2013).

[17] Chan, J. *et al.* Laser cooling of a nanomechanical oscillator into its quantum ground state. *Nature* **478**, 89–92 (2011).

[18] Stipe, B. C., Mamin, H. J., Stowe, T. D., Kenny, T. W. & Rugar, D. Noncontact Friction and Force Fluctuations between Closely Spaced Bodies. *Phys. Rev. Lett.* **87**, 096801 (2001).

[19] Yuen, H. P. & Chan, V. W. S. Noise in homodyne and heterodyne detection. *Opt. Lett.* **8**, 177–179 (1983).

[20] Schumaker, B. L. Noise in homodyne detection. *Opt. Lett.* **9**, 189–191 (1984).

[21] Shapiro, J. H. Quantum noise and excess noise in optical homodyne and heterodyne receivers. *IEEE J. Qantum Elect.* **21**, 237–250 (1985).

[22] Shelby, R. M., Levenson, M. D. & Bayer, P. W. Guided acoustic-wave brillouin scattering. *Phys. Rev. B* **31**, 5244 (1985).

[23] Levin, Y. Internal thermal noise in the LIGO test masses: A direct approach. *Phys. Rev. D* **57**, 659 (1998).

[24] Braginsky, V. B., Gorodetsky, M. L. & Vyatchanin, S. P. Thermodynamical fluctuations and photo-thermal shot noise in gravitational wave antennae. *Phys. Lett. A* **264**, 1–10 (1999).

[25] Liu, Y. T. & Thorne, K. S. Thermoelastic noise and homogeneous thermal noise in finite sized gravitational-wave test masses. *Phys. Rev. D* **62**, 122002 (2000).

[26] Gorodetsky, M. L. & Grudinin, I. S. Fundamental thermal fluctuations in microspheres. *J. Opt. Soc. Am. B* **21**, 697–705 (2004).

[27] Schliesser, A., Anetsberger, G., Rivière, R., Arcizet, O. & Kippenberg, T. J. High-sensitivity monitoring of micromechanical vibration using optical whispering gallery mode resonators. *New J. Phys.* **10**, 095015 (2008).

[28] Komma, J., Schwarz, C., Hofmann, G., Heinert, D. & Nawrodt, R. Thermo-optic coefficient of silicon at 1550 nm and cryogenic temperatures. *Appl. Phys. Lett.* **101**, 041905 (2012).